Desalination and Water Treatment
www.deswater.com

doi: 10.5004/dwt.2018.21850

112 (2018) 147–160
April

The wheat straw biochar research on the adsorption/desorption behaviour of mercury in wastewater

Shici Zhang[a], Mohammed A.S. Abdalla[b,c], Zejiao Luo[b,*], Shibin Xia[a,*]

[a]*School of Resources and Environmental Engineering, Wuhan University of Technology, Wuhan 430070, China, Tel. +86 153 9288 0268; email: xiashibin@126.com (S. Xia), Tel. +86 186 7238 0657; email: zhangshici@whut.edu.cn (S. Zhang)*
[b]*School of Environmental Studies, China University of Geosciences (Wuhan), Wuhan 430074, China, Tel. +86 134 7621 2088; email: zjluo@cug.edu.cn (Z. Luo)*
[c]*Department of Soil and Water Science, College of Agriculture, University of Bahri, Khartoum 1660, Sudan, Tel. +86 155 4907 1136; email: mohammed.akareem@gmail.com*

Received 20 July 2017; Accepted 23 December 2017

ABSTRACT

The adsorption/desorption behaviour and varying adsorption mechanisms of Hg(II) in simulated wastewater were evaluated using wheat straw biochars (WBCs) prepared under three different slow pyrolysis temperatures (300°C, 400°C, and 600°C, referred as WBC300, WBC400, and WBC600, respectively). The adsorption isotherm characteristics for these biochars were extensively described by the Langmuir isotherm ($R^2 > 0.9782$) and pseudo-second-order kinetics ($R^2 > 0.9421$) models, with the maximum theoretical adsorbing capacity measured at 5.85, 4.13, and 3.56 mg/g, respectively, in the following order: WBC300 > WBC400 > WBC600. The experimental results showed that there was a direct competitive adsorption in Pb(II) and Hg(II) binary system, whereas not in Cd(II) and Hg(II) system. The Hg(II) desorption behaviour on the surface of these biochars, confirmed by the FTIR results and water-soluble cations test, which indicated that the low temperature biochars (WBC300 and WBC400) adsorbed Hg(II) mainly relied on complexation reactions with oxygen-containing functional groups such as carboxyl, alcoholic and phenolic hydroxyl, while high temperature biochars (WBC600) mainly relied on ion-exchange interactions. This research proposes an efficient, environmentally friendly, and economical method for mercury-containing wastewater remediation and simultaneous agriculture residue treatment.

Keywords: Wheat straw; Biochar; Mercury-containing wastewater; Adsorption; Desorption

1. Introduction

Mercury (Hg) known as one of the high toxicity heavy metals, and exist mainly in the gaseous phase in the global environmental chemical cycle, which potentially inducing health issues that lead to poisoning, and other human diseases [1]. Mercury is present in the environment in three forms: elemental mercury (Hg^0), inorganic mercury (Hg^+ and Hg^{2+}), and organic mercury. Among them, Hg^{2+} is predominantly can be transformed to methylmercury which may cause nervous system damage due to the inhalation or bioaccumulation through food chain [2–4]. Mercury can also be released into the aquatic environments via natural and anthropogenic processes. For artificial emission pathways, including coal combustion, chlor-alkali processing, mining, oil refining, electroplating, and battery, paint, and paper manufacturing [5,6]. However, in the awareness of its health hazards and contaminant issues, the United Nations Environment Programme (UNEP) led the Minamata Convention concerning mercury in 2013 [7], and China as one of the signatories, agreed to

* Corresponding author.

Presented at the 5th International Conference on Sustainable Solid Waste Management (ATHENS 2017), 21–24 June 2017, Athens, Greece.

regulate the mercury emission limits of existing facilities to be raised from 0.02 to 0.005 mg/L, while it should be less than 0.001 mg/L for environmentally vulnerable areas that effective on January 1st of 2016, according to the Emission Standard of Pollutants for Battery Industry (GB 30484-2013). Several techniques for the removal and regulation of mercury emissions in aquatic environments are already available, including chemical precipitation (coprecipitation, sulphide precipitation, etc.) [8,9], electrolytic method via electrocoagulation [10,11], ion-exchange procedures [12,13], and other biological methods [14,15], but among them, such downsides as the need for relatively long reaction time, production of solid residues, and the cause of secondary contamination [16] limited their development possibility. Moreover, physical and chemical adsorption techniques are currently garnering attention in the research field as it makes use of a simple device and operation process with the most common adsorbent being activated carbon (AC) as well as its derivatives which were proved to be efficient in mercury adsorption [4,17,18]. However, the large-scale industrial application of these AC adsorbents is blocked due to their complex activation process, high energy consumption and crude material cost, even the low selectivity [19].

Different from AC, biochar is produced via thermal pyrolysis with limited oxygen or inert gas conditions under relatively low temperature (less than 700°C). The characteristics of biochar such as porous, carbon-rich, fine-grained, and bearing a variety of chemical composition and surface functional groups are related to its production environment and raw material (naturally renewable biomass) generation, which can be divided into crop straw, wood, poultry manure, animal bones, and so on, thereby further affecting the adsorption performance of the substance [20–25]. In China, the total yield of straw ranked first all around the world with an annual output of more than 800 million tons, in which global wheat straw production occupied in an estimated rate of more than 12% [26], regarded as desirable biochar precursor. Recently, the evolution of biochar from AC alternative to the pyrolytic black carbon adsorbent, received a increasing attention with a view of its bargain price, high efficiency and environmentally friendly traits in heavy metal-containing wastewater remediation, majorly focusing on Pb(II), Cd(II), Ni(II), Cu(II), and As(V) [27–31]. Hanandeh et al. [32] prepared biochar from Jordanian olive oil processing solid waste and found that the adsorption capacity of Hg(II) have increased with the improvement of its pyrolysis temperature, therefore, the resulting maximum capacity was 104.59 mg/g with a terminal temperature of 630°C. However, the Brazilian pepper biochar reflected an opposite tendency by which the higher the pyrolysis temperature generated, the lower the resulting Hg(II) adsorption capacity. In this matter, the maximum capacity occurred at 24.2 mg/g with a biochar pyrolysis temperature of 300°C [5]. This indicated that the biochar adsorption capacity showed a relationship with the sources of biomass and the initial mercury concentration, but Hg(II) adsorption behaviour onto biochar prepared at different pyrolysis temperatures using wheat straw as a precursor has not been reported. On the other hand, Xu et al. [33] compared Hg(II) adsorption characteristics and mechanisms of two biochars which were obtained from dried bagasse and hickory chips pyrolyzed at 450°C for 2 h and another commercial AC. Their results showed that biochars had better adsorption capabilities than AC by the substances' complexation and Hg–π binding with functional groups. Nevertheless, the distinguishing Hg(II) adsorption mechanism of different temperature wheat straw biochars (WBCs) was barely investigated, especially under desorption behaviour. In the case of coadsorption of phenanthrene and mercury, Kong et al. [34] and Tang et al. [35] investigated soybean stalk-based and graphene biochar, respectively, their findings concluded that biochar still evidently revealed prospects in the coadsorption application despite the polycyclic aromatic hydrocarbon and mercury bearing a competitive adsorption mechanism in the binary solution. Based on such binary system, the adsorption behaviour of WBC on Hg(II) containing mixed other heavy metal wastewater systems ought to be studied.

As discussed in the above review, the overall objective of this research is to explore and elaborate the varying mechanisms of Hg(II) adsorption at different temperature (300°C, 400°C, and 600°C) WBCs through a series of adsorption/desorption experiments in batch and binary system, to further investigate the pH_{PZC}, surface functional groups, and water-soluble cations in the simulated wastewater systems. In this study, the acquisition of such WBCs was used for the integration of agricultural residual biomass management towards industrial heavy metal wastewater treatment.

2. Materials and methods

2.1. Preparation of wheat straw biochars

Fresh wheat straw (variety: Zhengmai No.3) was collected from Hannan district, Wuhan, China (114.04°E, 30.29°N). Samples were washed three times to remove surface dust or insect debris, then oven-dried (DHG-9240A, Sanfa Scientific Instruments Co., Ltd., China) at 105°C for 12 h. Then, the straw was fed into the vacuum tube furnace (TF-1200X, Hefei Ke Jing Materials Technology Co., Ltd., China) and the pyrolysis temperature was adjusted to reach the specified temperature (300°C, 400°C, and 600°C, respectively) at the heating rate of 10°C/min which was then maintained on the entire procedure for up to 2 h. During the production of the biochars, the N_2 was continuously induced into the furnace at a flow rate of 60 mL/min to maintain the oxygen-free environment. The biochars were then cooled at the room temperature and passed through 60 mesh sieve (less than 0.25 mm), referred as BC300, BC400, and BC600.

2.2. Characterization of wheat straw biochars

The physicochemical properties of the BC samples were studied including the yield, net yield (Eqs. (1) and (2)), ash content, and pH according to the National Standards of People's Republic of China GB/T 12496.3-1999 and GB/T 12496.7-1999, respectively. In brief, for the ash content calculation, 1 g of each biochar was added into 30 mL porcelain crucible and gradually heated up to 650°C ± 20°C, then ashing to a constant weight (Eq. (3)). For pH determination, 2.50 g sample was weighted and mixed with 50 mL deionized water, then the sample was filtrated and the filtrate was tested by pH meter.

Scanning electron microscopy (SEM; SU8010, Hitachi, Japan) was employed for the surface morphology scanning. The Brunauer–Emmett–Teller model (BET; Tristar II 3020, Micromeritics, USA) was used to determine the specific surface area with the N_2 adsorption/desorption isotherm carrying out at 77.3 K. The chemical elements of the BCs were analyzed through X-ray fluorescence (XRF; ZSX Primus II, Rigaku, Japan), by using boric acid as the tabletting substrate with its testing voltage and current being 50 kV and 60 mA, respectively. X-ray diffraction (XRD; X'Pert Powder, PANalytical, Netherlands) was used to investigate the crystallization of the BC samples, and the conditions were set as Cu Kα, 40 kV, 40 mA. The scanning peaks were collected in the range of 5°–80°, then the analysis of the data was done through MDI Jade 6.0. According to the XRF test results, the main soluble alkali and alkaline earth metals (K^+, Na^+, Ca^{2+}, and Mg^{2+}) were measured through the following steps: (1) Accurately weighing the BC sample of 1.00 g which was then mixed with 20 mL deionized water. (2) Oscillation was done at 25°C and 210 rpm for 24 h, then filtered through 0.25 μm. (3) Testing by flame atomic absorption spectrophotometer (FAAS; TAS-990, Persee, China), following the National Standards of People's Republic of China GB/T 11904-89 and GB/T 11905-89.

$$\text{Yield}(\%) = \frac{\text{Biochar weight}}{\text{Wheat straw weight}} \times 100 \quad (1)$$

$$\text{Net yield}(\text{g/g}) = \frac{\text{Yield} \times (1 - \text{ash content})}{1.0000} \quad (2)$$

$$\text{Ash content}(\%) = \frac{\text{Ash and crucible weight} - \text{original crucible weight}}{\text{Biochar sample weight}} \times 100 \quad (3)$$

2.3. Batch adsorption/desorption experiments

This experiment was conducted to the washed BCs by deionized water, then dried at 105°C for 12 h and referred to WBC300, WBC400, and WBC600. The simulated mercury-containing wastewater prepared using $Hg((NO)_3)_2$ with the Hg(II) initial concentration of 2 mg/L, and the background ion strength was 0.01 M $NaNO_3$. All the experiments were performed in triplicate, with the WBC dosage of 0.03 g per 50 mL Hg(II) solution in centrifuge tubes which were then oscillated at 25°C, 210 rpm for 24 h, and further filtered with a 0.25 μm membrane. For mercury concentration testing, the atomic fluorescence spectrometer (AFS, AFS-9700, Haiguang Instrument Co., Ltd., China) was used with the following conditions: negative pressure of photomultiplier tube being 300 V, lamp current at 30 mA, carrier agent and reducing agent at 5% HNO and 10% KBH_4, respectively, followed the Environmental Protection Standards of the People's Republic of China HJ 694-2014.

2.3.1. Effects of pH

The pH of simulated wastewater was adjusted using 0.1 M HNO_3 and NaOH to reach the ranges from 2.0 to 11.0. The residual mercury concentration in the solutions was then tested by AFS after the adsorption reaction.

2.3.2. Isotherm studies

Different Hg(II) concentrations (0.1, 0.5, 1, 2, 4, 6, 8, and 10 mg/L) were prepared to investigate the adsorption isotherms on WBC surface at pH = 6. Mercury removal rate η (%) and uptake capacity q_t (mg/g) of WBC300, WBC400, and WBC600 after adsorption equilibrium were calculated as Eqs. (4) and (5). The data were fitted into Langmuir (LM) and Freundlich (FD) empirical isotherm models as shown in Eqs. (6)–(8).

$$\eta = \frac{C_0 - C_t}{C_0} \times 100\% \quad (4)$$

$$q_t = \frac{C_0 - C_t}{m} V \quad (5)$$

$$\text{Langmuir equation: } q_e = \frac{K_L q_m C_e}{1 + K_L C_e} \quad (6)$$

$$K_R = \frac{1}{1 + K_L C_0} \quad (7)$$

$$\text{Freundlich equation: } q_e = K_F C_e^{1/n} \quad (8)$$

where C_0, C_t, and C_e are the initial, t time, and adsorption equilibrium concentration of simulate mercury-containing wastewater, respectively (mg/L), m is WBC dosage (0.03 g), V is solution volume (50 mL), q_e is equilibrium adsorption capacity (mg/g), K_L is LM constant (L/mg), q_m is maximum adsorption capacity (mg/g), K_R is a dimensionless parameter, K_F is FD constant (L/g), and $1/n$ is another dimensionless parameter.

2.3.3. Kinetic studies

To perform the adsorption kinetics study, a conduct of an estimated test of the remaining Hg(II) concentration in equilibrium conditions at prescribe time intervals (1, 5, 10, 20, 30, 40, 60, 120, 180, 240, 480, 600, 720, 900, and 1,440 min) was considered and then fitted into the pseudo-first-order and pseudo-second-order model:

$$\text{Pseudo-first-order equation: } q_t = q_e\left[1 - \exp(-k_1 t)\right] \quad (9)$$

$$\text{Pseudo-second-order equation: } q_t = \frac{k_2 q_e^2 t}{1 + k_2 q_e t} \quad (10)$$

where q_e is equilibrium adsorption capacity (mg/g), q_t is adsorption capacity at t time (mg/g), k_1 and k_2 are rate constant for the pseudo-first-order adsorption (1/min) and pseudo-second-order adsorption (g/(mg·min)), respectively.

2.3.4. Static desorption experiments

WBC was separated from the solution after the adsorption experiment (with initial Hg(II) concentration of 2 mg/L), then the equilibrium adsorption capacity q_e (mg/g) was calculated by testing the remaining mercury concentration in the filtrate. The above WBC samples were then added into three kinds of desorption solutions namely deionized water, 0.01 M HNO_3 and $NaNO_3$ at pH = 6, and oscillated at 25°C, 210 rpm for 24 h. After the reaction and filtration, desorption capacity q_d (mg/g) and desorption rate η (%) were obtaining using the following Eqs. (11) and (12):

$$q_d = \frac{C_d}{m} V \tag{11}$$

$$\eta = \frac{q_d}{q_e} \times 100\% \tag{12}$$

where C_d is equilibrium desorption capacity (mg/L), m is WBC dosage (0.03 g), V is solution volume (50 mL).

2.3.5. Adsorption in binary wastewater system

A batch concentrations of metallic ions Cd(II) and Pb(II) in the solution ranged from 0.1 to 10 mg/L were found from their nitrates and coexisted with 2 mg/L Hg(II) at pH = 6 for the formation of a binary system respectively. One of the most efficient WBC sample was chosen to explore the capture capability of Hg(II) in the mixed simulated wastewater. Testing of the Cd(II) and Pb(II) concentration followed the National Standards of People's Republic of China GB 7475-87.

2.4. Investigation of adsorption mechanism on mercury by wheat straw biochars

The surface functional groups of WBCs were investigated before and after adsorption equilibrium by Fourier-transform infrared spectrometer (FTIR; Tensor27, Bruker, Germany). The samples were mixed with KBr powder and compressed tablets. The FTIR was recorded with a 0.6 cm^{-1} resolution and 4,000–600 cm^{-1} infrared domain. The pH_{PZC} (point of zero charge) of WBCs was determined as described in the previous researches [36,37]. The concentration changes of the main soluble metallic ions (K^+, Na^+, Ca^{2+}, and Mg^{2+}) were measured before and after the adsorption equilibrium of 20 mg/L Hg(II) with a pH of 6, and WBC dosage of 0.3 g without setting the ion strength, then followed as mentioned in steps (2) and (3) in section 2.2.

3. Results and discussion

3.1. Characterization of wheat straw biochars

The main physical and chemical properties of BCs pyrolyzed at 300°C, 400°C, and 600°C are presented in Table 1. The ash content and pH values were increased with the pyrolysis temperature growing, making BC600 as high as 30.54% and 10.58, respectively due to the non-pyrolyzed inorganic compounds accumulated in wheat straw. Nevertheless, low temperature BC showed a higher yield because of the minimal condensation of aliphatic compounds and less loss of

Table 1
Physical and chemical properties of BCs

BCs	The yield, ash content, net yield and pH of biochars				The textural parameters of biochars									
	Yield (%)	Ash content (%)	Net yield (g/g)	pH	S_{BET} (m^2/g)	S_{BET} of micropore (m^2/g)	Micropore volume (cm^3/g)	S_{BET} of mesopore (m^2/g)	Mesopore volume (cm^3/g)	Total pore volume (cm^3/g)	Average pore size (nm)			
BC300	51.62	18.17 ± 0.76	0.42 ± 0.00	7.55 ± 0.36	2.77	N.A.	N.A.	1.00	0.0082	0.0083	17.13			
BC400	37.25	21.77 ± 0.80	0.29 ± 0.00	8.54 ± 0.16	5.33	0.93	0.0003	2.34	0.0093	0.0167	12.87			
BC600	34.03	30.54 ± 1.22	0.24 ± 0.00	10.58 ± 0.41	55.92	39.47	0.0184	7.38	0.0101	0.0320	6.09			
BCs	The relative content of elements tested by XRF (wt%)													
	K	Ca	Mg	Na	Fe	Mn	Al	Zn	Si	Cl	S	P		
BC300	39.27	12.75	1.00	0.09	0.53	0.21	0.23	N.A.	36.43	4.89	2.73	1.87		
BC400	38.98	14.49	1.17	0.06	0.65	0.25	0.23	0.12	35.51	3.78	2.35	2.41		
BC600	36.96	11.08	1.26	0.10	0.67	0.24	0.31	0.16	40.19	3.80	2.23	3.00		
BCs	The content of water-soluble cations (mg/g)				The element content (%) and atomic ratio									
	K^+	Na^+	Ca^{2+}	Mg^{2+}	C	H	O	N	S	H/C	O/C	(O + N)/C		
BC300	14.08 ± 0.29	0.28 ± 0.06	0.47 ± 0.06	0.15 ± 0.03	54.92	2.80	22.24	0.62	0.55	0.61	0.30	0.31		
BC400	17.85 ± 0.12	0.30 ± 0.07	0.51 ± 0.07	0.10 ± 0.02	58.20	1.66	18.69	0.60	0.63	0.34	0.24	0.25		
BC600	34.03 ± 3.43	0.30 ± 0.06	0.79 ± 0.07	0.27 ± 0.07	61.31	0.84	11.45	0.51	0.68	0.16	0.14	0.15		

volatile gas [38]. It could be indicated that high temperature BC was more carbonized and dehydrated with polyaromatic structure formation due to the increased content of C and decreased contents of H, O, H/C, O/C, and (O + N)/C ratios as the pyrolysis temperature increasing, of which the reduction of O/C and (O + N)/C demonstrated the decline of surface polar functional groups generally with the decrease of surface acidity [39,40]. For XRF results, K and Ca accounted for the largest proportions of metallic elements in BCs (52.02, 53.47, and 48.04 wt% for BC300, BC400, and BC600, respectively), while Si accounted for the highest amount of the non-metallic elements (36.43, 35.51, and 40.19 wt% for BC300, BC400, and BC600, respectively) due to its strong ability to absorb nutrients like silicon in soil for crop growth and yield improvement, also it would not loss during pyrolysis process as temperature increased [41]. The results indicated that the concentrations of water-soluble K^+, Na^+, Ca^{2+}, and Mg^{2+} increased as pyrolysis temperature enhanced. Among them, K^+ occupied the highest proportion which echoed XRF results. These cations mainly came from alkali dissolutions and likely competed for the negatively charged points on biochar surface with heavy metals resulting to the decreased adsorption efficiency. Based on these elemental determinations, XRD analysis was performed (Fig. 1), and the spectra showed that there were no obvious crystal substances presented in this kind of WBCs, but only silica (SiO_2, diffraction peaks at 28.14°) and potassium sulphate (K_2SO_4, diffraction peaks at 29.55°, 30.39°, and 40.53°) were found in their subcrystalline forms, with more prominent crystallization and higher diffraction peaks of silica at increased pyrolysis temperatures. This was analogous to the changes in the XRD spectra of a corn straw biochar, as reported by Yuan et al. [42], no crystals were observed at 300°C samples, further the presence of calcite ($CaCO_3$), dolomite ($CaMg(CO_3)_2$), and sylvite (KCl) peaked at 3.03, 2.90, and 3.15 Å, respectively, at a pyrolysis temperature of 500°C, which were confirmed by several more peaks forming at 700°C. Thus, it could be concluded that the crystalline mineral components of such agriculture residue biochars are not abundant.

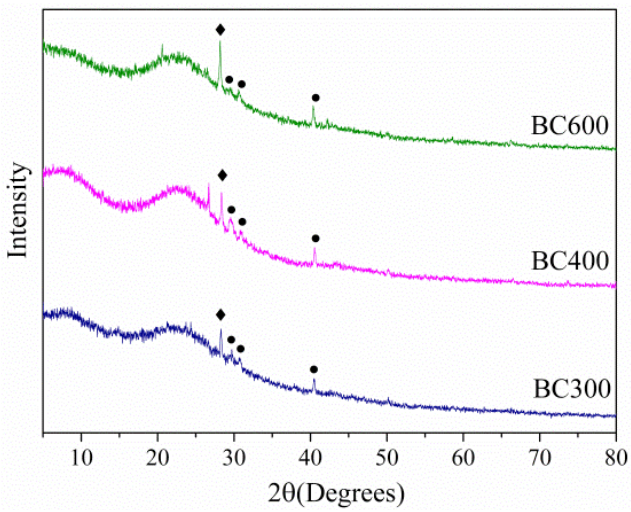

Fig. 1. The X-ray diffraction spectra for BCs (◆ silica, SiO_2; ● potassium sulphate, K_2SO_4).

For textural characteristics (Table 1), the S_{BET} had a rapid increase from 5.33 m^2/g for BC400 to 55.92 m^2/g for BC600. The micropore development in BC600 could be verified by relatively high S_{BET} value in the micropore (39.47 m^2/g) and low value of the average pore size (6.09 nm). According to the N_2 adsorption/desorption curves (Fig. 2), the Type II shape of the IUPAC classification was followed by these three plots. It also displayed an H4 hysteresis loop [43], which was related to the typical single to multi-layer adsorbing carbon materials. When P/P_0 was in the lower pressure range of 0–0.3, BC600 expressed an anti-S type for the N_2 adsorption curve with a significant increase of absorbance which indicates the microporous structure bearing a diameter of less than

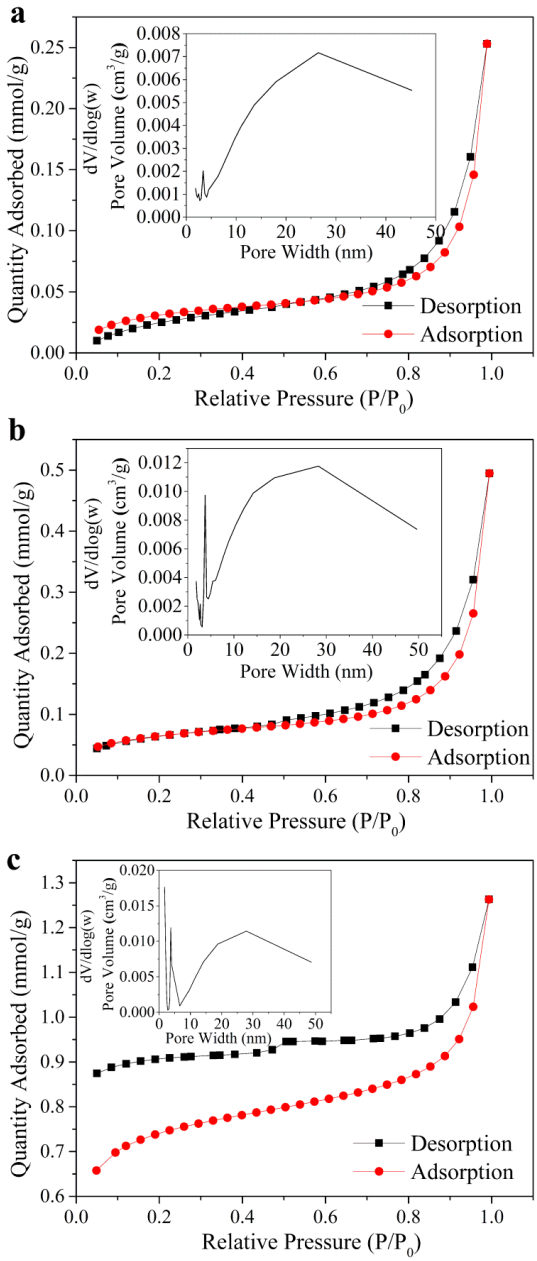

Fig. 2. N_2 adsorption/desorption isotherms and corresponding pore size distribution plots of (a) BC300, (b) BC400, and (c) BC600.

2 nm in the BC. In addition, the occurrence of a multi-layer adsorption was in the high pressure range of 0.8–1.0. The first increscent in the N_2 adsorption capacity in three BCs indicating the textural structure mainly consisted of mesopores which could be proved by pore size distribution curves (Fig. 2), in which the pore width almost distributed between 2 and 50 nm. The adsorption capacity of these three BCs ordered as BC600 > BC400 > BC300 when P/P_0 was close to 1 which demonstrates the increasing of pyrolysis temperature provided positive benefits to the development of porosity and total pore volume [44,45]. The morphology was observed that the textural properties were gradually changed with the different charring temperatures (Fig. 3). The formation of the bundle-shaped tube on BC300 created uneven sized pores bearing a diameter range between 5 and 8 μm. On the other hand, the pores of BC400 were more well-distributed. Compared with the low temperature BCs, BC600 possessed a neater tubular structure and thinner pore walls which led to bearing a larger pore opening (15–18 μm). As the enlargement of (c2) and (c3) showed smaller pores generated that consistent with the previous textural parameters results. Tiny carbon slices or ash particles were clearly adhered to the surface of the BC inhomogeneously, which could block the pores on the surface of biochars and the dissolved alkalinity that could affect the pH values of adsorbate solutions [46], thus influencing the Hg(II) removal efficiency. Based on this observation, these particles could be removed by deionized water or acid solutions [47,48]. However, the S_{BET} of biochar materials is much lower than ACs derived from agriculture biomass materials (Table 2) which further differing the mechanism of heavy metal adsorption, that is to say the surface pore adsorption might not be the main mechanism of biochars, especially for low temperature biochars [5,49].

3.2. Effects of initial pH on Hg(II) removal efficiency

The interaction between Hg(II) ions and biochar depends on the pH of the solution as it affects metal speciation, surface charges and mineral components dissolution of adsorbent. Since pH is an important parameter, prior to conduct this experiment, biochars were washed by the deionized water (WBC) to avoid alkalinity impact on initial pH. The tendency of Hg(II) adsorption efficiencies at three pyrolysis temperatures was almost the same (Fig. 4). An increase in the removal efficiency of Hg(II) was directly proportional to the pH values within a range of 2.0–6.0, where the maximum rate of increase occurred at 2.0–3.0. It seems that $Hg(OH)^+$ and Hg^{2+} were the dominant species (≥70%) of mercury in solution at pH 2.0–3.0 [5], while the surface of WBCs was protonated. Therefore, it could be concluded that there was a repulsive force between the WBCs and mercury-containing cations, which further decreased mercurial adsorption on the surface and pores of biochar. On the other hand, alkali and alkaline earth metals (K^+, Na^+, Ca^{2+}, and Mg^{2+}) dissolved in strong acid solutions with large numbers of H^+ and caused competition in the adsorption with mercury-containing cations, resulting in lower removal efficiency. Then, with a continuous increase in pH, the removal efficiency of WBC300 and WBC400 reached a plateau at a pH range of 6.0–8.0, further decreased as pH went up to 11.0, whereas the removal efficiency of WBC600 maintained a downward trend from pH 6.0 to 11.0. Hereinto, the maximum removal efficiency obtained at pH 6 was 97.1%, 94.3%, and 90.2% for WBC300, WBC400, and WBC600, respectively. In neutral and alkalescency environments, competitive adsorption was less prominent due to the decrease in metallic cation concentration and deprotonation of the biochar surface as pH gradually rising up [54]. When pH changed to strong alkaline, $Hg(OH)_2$ was formed via the increased concentration of OH^- and the hydrolysis of Hg(II), which reduced the freedom degree of mercury, making it unfavourable to adsorption, but the result was much desired than strong acid condition might be due to the $Hg(OH)_2$ precipitation. To consolidate the above analysis, the subsequent experiments were all carried out at pH 6.0, which was proposed by previous researches that highest Hg(II) adsorption capacity occurred at a pH range of 4–6 [32].

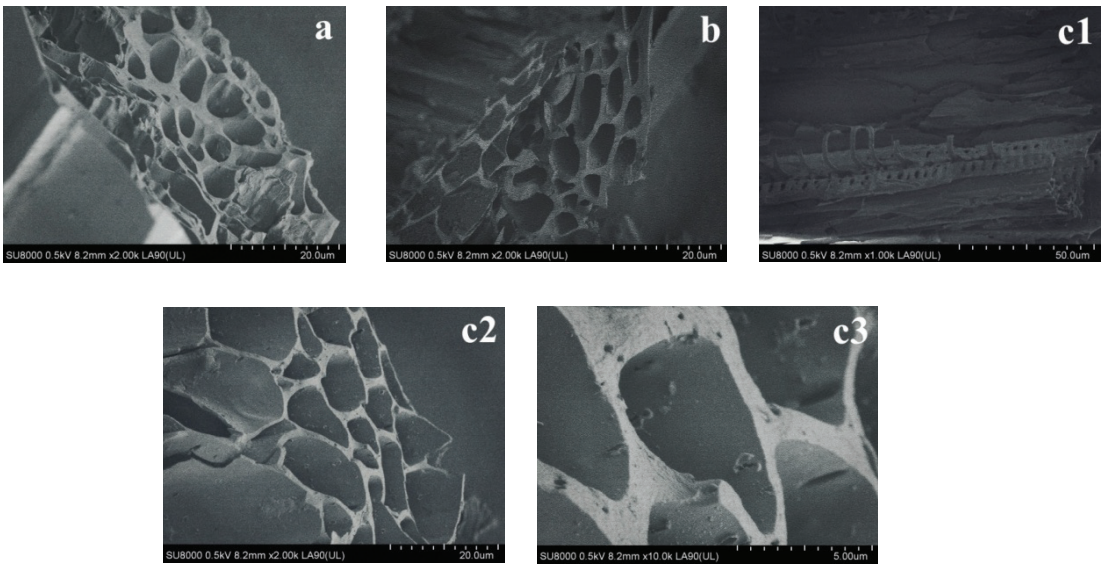

Fig. 3. SEM images of BCs (a) BC300 × 2.00k, (b) BC400 × 2.00k, (c1) BC600 × 1.00k, (c2) BC600 × 2.00k, and (c3) BC600 × 10.0k.

Table 2
Summary of S_{BET} to BC and AC materials

	Raw material	Pyrolysis temperature (°C)/activation process	S_{BET} (m^2/g)	Reference
BC	Wheat straw	650–850	34	[50]
	Wheat straw	600	65.151	[51]
	Corn straw	500	32.85	[1]
	Bagasse	450	15.3	[33]
	Peanut shell	300	3.75	[49]
		400	4.57	
		600	5.57	
	Wheat straw	300	2.77	This paper
		400	5.33	
		600	55.92	
AC	Wheat straw	650–850/molten salt	544	[50]
		750/molten salt with $LiNO_3$	1,067	
	Wheat straw	Activated at 1,250°C	197	[52]
		Activated at 1,500°C	167	
	Coconut shell	–	922	[33]
	Corn straw	800/pretreated with KOH	466.37	[1]
	Rice straw	900/mixed with K_2CO_3	2,034–2,197	[53]

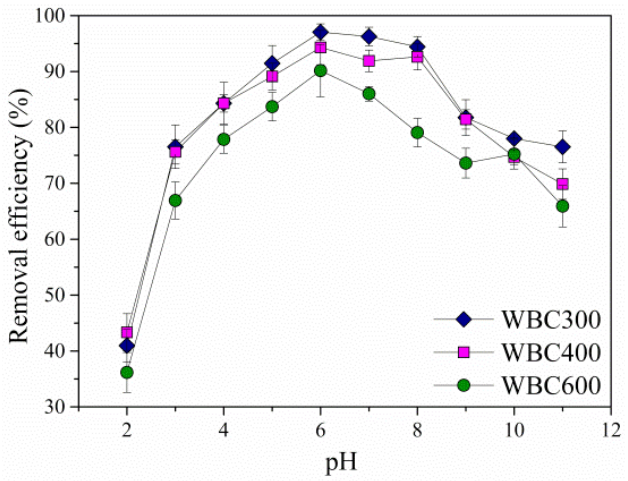

Fig. 4. Effects of initial pH on Hg(II) removal efficiency.

3.3. Adsorption isotherms

Adsorption isotherms provide a means of evaluating the maximum adsorption capacities of adsorbent and the applicability of a complete adsorption operation through a proceeding until the remaining adsorbate existing in the equilibrium solution system. Moreover, the fitting of adsorption isotherm models reflects the interaction mechanisms between the adsorbent and the adsorbate [55].

The non-linear fits to the LM and FD empirical isotherms of experimental data are depicted in Fig. 5, and the isothermal parameters are listed in Table 3. The correlation coefficient value R^2 estimates the fitness to isotherm models, as observed, the R^2 of LM was close to FD for WBC300, meanwhile all three isotherms were fitted more with LM model. Similar phenomenon occurred at WBCs [35], malt spent rootlets biochars [6], and soybean stalk-based biochars [34], that LM isotherm model was more suitable for describing the adsorption process of Hg(II) than FD isotherm. As per theoretical foundation, the LM isotherm model assumes that adsorbent surface is a homogeneous monolayer with a limited amount of adsorption active sites, and each adsorbate molecule bonds to one site until all of them are occupied to reach its maximum adsorption capacity (q_m) [56]. The theoretical q_m determined from LM model was 5.85, 4.13, and 3.56 mg/g for WBC300, WBC400, and WBC600, respectively, which was close to the experimental values 6.05, 4.27, and 3.59 mg/g with standard deviation were 14.14%, 9.90%, and 2.12%, respectively, showing that q_m are ranked as WBC300 > WBC400 > WBC600. In addition, the dimensionless parameter K_R indicates the type and favourability of isotherms, dividing it into unfavourable ($K_R > 1$), linear ($K_R = 1$), favourable ($0 < K_R < 1$), and irreversible ($K_R = 0$) [57]. From Table 3, K_R were all within the range of 0–1, implying a favourable adsorption of Hg(II) on WBCs. It is worth to be mentioned that the higher the initial Hg(II) concentration, the smaller the K_R value, and the more favourable it would be to the adsorption process. The analogical conclusion could be derived from FD parameter $1/n$, where a value between 0 and 0.5 manifests that the Hg(II) was facile to be adsorbed on WBCs ($1/n$ = 0.1740–0.2225 for WBCs) [54].

3.4. Adsorption kinetics

The adsorption of Hg(II) onto WBCs can be divided into two stages (Fig. 6): (1) a rapid stage took place within the first 10 min where the removal rate and adsorption capacity reached its largest increase, (2) after that, slow stage showed a gentle adsorption increase rate until equilibrium reached 240 min for WBC300 and WBC400, 360 min for WBC600. The pseudo-second-order kinetic model presented a higher R^2

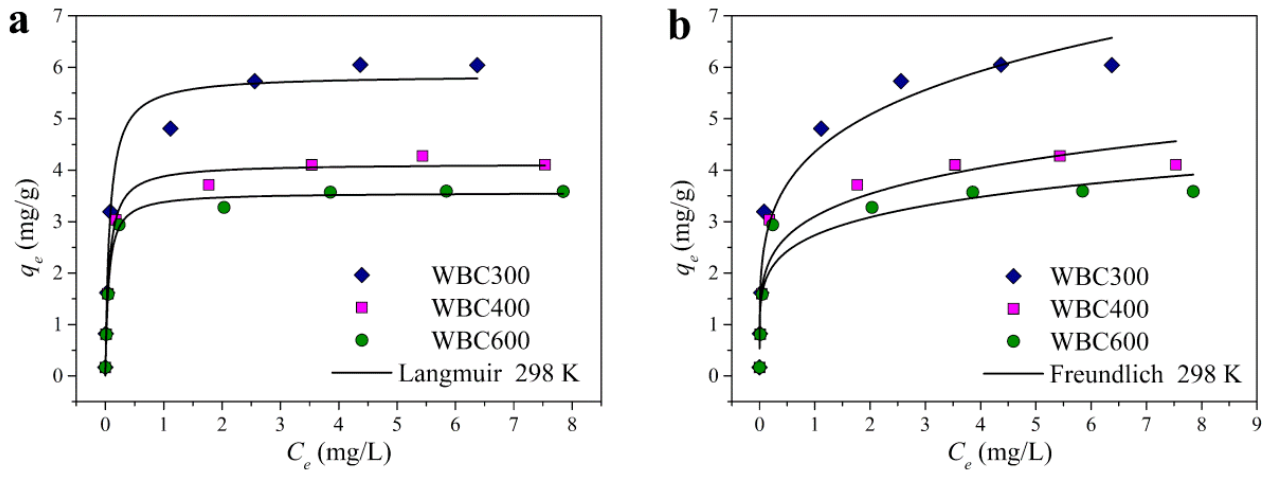

Fig. 5. Non-linear fits of (a) Langmuir and (b) Freundlich isotherm models of Hg(II) adsorption on WBCs.

Table 3
Adsorption isotherm and kinetics parameters for Hg(II) removal on WBCs at 298 K

WBCs	$q_{m,exp}$ (mg/g)	Langmuir isotherm model				Freundlich isotherm model		
		$q_{m,the}$ (mg/g)	K_L (L/mg)	K_R	R^2	K_F (L/g)	$1/n$	R^2
WBC300	6.05 ± 0.24	5.85	13.66	0.0073–0.4227	0.9782	4.35	0.2225	0.9543
WBC400	4.27 ± 0.10	4.13	15.67	0.0063–0.3895	0.9909	3.10	0.1915	0.9090
WBC600	3.59 ± 0.30	3.56	18.12	0.0055–0.3556	0.9932	2.73	0.1740	0.8912
WBCs	$q_{e,exp}$ (mg/g)	Pseudo-first-order kinetic model			Pseudo-second-order kinetic model			
		k_1 (min^{-1})	$q_{e,the}$ (mg/g)	R^2	k_2 (g/mg/min)		$q_{e,the}$ (mg/g)	R^2
WBC300	3.28 ± 0.15	0.15	3.13	0.8772	0.08		3.27	0.9894
WBC400	3.10 ± 0.08	0.14	2.86	0.9601	0.06		3.07	0.9964
WBC600	2.98 ± 0.01	0.03	2.94	0.8557	0.02		3.14	0.9421

Note: "exp" is experimental value and "the" is theoretical value.

for the three biochars, and the theoretical equilibrium capacity $q_{e,the}$ (3.27, 3.07, and 3.14 mg/g for WBC300, WBC400, and WBC600, respectively) was close to the experimental value $q_{e,exp}$ (3.28, 3.10, and 2.98 mg/g for WBC300, WBC400, and WBC600, respectively), with corresponding standard deviations of 0.71%, 2.12%, and 11.31% (Table 3). This implies that the adsorption of Hg(II) by WBCs was not only determined by a single factor, but by a variety of mechanisms, and that the main rate determining step was controlled by chemical adsorption, involving surface adsorption and valence forces such as ion or electron exchange [57,58]. As for k_2 values of these three biochars were ranked in the order WBC300 ≈ WBC400 > WBC600, indicating the adsorption rates of first two WBCs were greater than WBC600 and that was the reason why the former reached adsorption equilibrium more faster, which was consistent with the practical situation.

3.5. Desorption of Hg(II) in different agents

Desorption study provides a method to explore the usability of adsorbent and further investigating the adsorption mechanism. Generally, inorganic acid agents desorb the heavy metal ions by increasing the concentration of H^+ which could combine with the surface functional groups of adsorbents. Inorganic salt agents have a similar desorption mechanism with inorganic acids that large amounts of cations are introduced into solution, which seize the adsorption sites by exchanging ions with Hg(II). Although deionized water is used as a low-cost desorbent agent, it could only separate Hg(II) adsorbed by physical forces such as electrostatic interaction and van der Waals forces between molecules, but has little effect on Hg(II) adsorbed chemically. It could be seen from Fig. 7 that the desorption efficiencies of three desorbing agents on WBC300 and WBC400 are ranked as HNO_3 > $NaNO_3$ > H_2O. Acidic solutions were proved to be the most efficient in the desorption of Hg(II) from biochars with a desorption capacity of 1.03 and 1.03 mg/g and a desorption rate of 30.9% and 31.5% for WBC300 and WBC400, respectively. This indicates that the mechanisms of Hg(II) adsorption onto biochar might be complexation reaction with its functional groups. In contrast to the desorption effect of the three biochars in the similar agent, it was found that the desorption capacities and rates of WBC600 in H_2O and $NaNO_3$ were higher than that of low pyrolysis temperature biochars with values up to 0.84 mg/g and 26.8%, respectively,

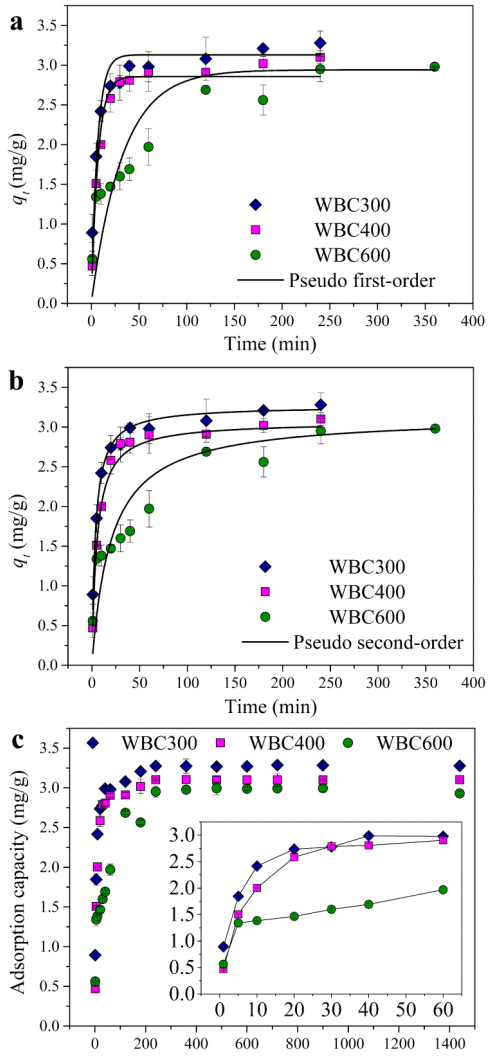

Fig. 6. Non-linear fits of (a) pseudo-first-order, (b) pseudo-second-order kinetics models of Hg(II) adsorption on WBCs, and (c) adsorption capacity of WBCs at different times.

but was slightly lower in HNO_3. It could be speculated that the WBC600 did not mainly rely on the complexation reactions to adsorb Hg(II), otherwise the electrostatic or ion-exchange reactions might be the dominating mechanism. In addition, the overall desorption rates of three agents were less than 50%, which was due to the limited concentration of desorption agents [59].

3.6. Competitive adsorption of Hg(II) in binary systems

As mentioned above, the WBC300 had a relatively larger adsorption capacity among the three biochars. In this part, WBC300 was used to probe the competitive adsorption efficiency of Hg(II) in Hg–Cd and Hg–Pb binary systems. Fig. 8 shows that with an increase in the initial concentration of Cd(II), the removal rate of Hg(II) was stable at about 95%, while the removal efficiency of Cd(II) was more than 99% with an initial concentration from 0.1 to 5 mg/L, and when further improved to 10 mg/L, the removal efficiency reduced to 70.9% with an increasing adsorption capacity of Cd(II) onto WBC300 which reached 11.81 mg/g. However, the WBC300 in Hg–Pb binary system showed a rather different result. For a higher initial concentration of Pb(II) at 10 mg/L, the removal efficiency of Pb(II) was only 73.0% with adsorption capacity of 12.26 mg/g, and Hg(II) removal rate suddenly decreased to 77.2% which indicates that there was a competition adsorption between Pb(II) and Hg(II), but no obvious impact between Cd(II) and Hg(II).

In order to further investigate the dynamics of adsorption behaviour in binary systems, q_e'/q_e ratios were utilized for calculations (q_e' and q_e are equilibrium uptake capacities in binary and single systems, respectively), when $q_e'/q_e > 1$ indicates that the equilibrium adsorption capacity of heavy metal ions in the binary system is larger than that of the single system, meaning the coexisting ions have synergistic effect on adsorption; on the contrary, $q_e'/q_e < 1$ indicates antagonism effect between coexisting heavy metal ions; $q_e'/q_e = 1$ indicates coexisting ions have no interaction to adsorbent compared with single systems [60]. Hg(II), Cd(II), and Pb(II) were the main adsorbates ordinally and their ratio values are shown in Table 4. The q_e'/q_e for Hg–Pb and Pb–Hg binary systems were 0.81 and 0.97, respectively, which implies that antagonistic

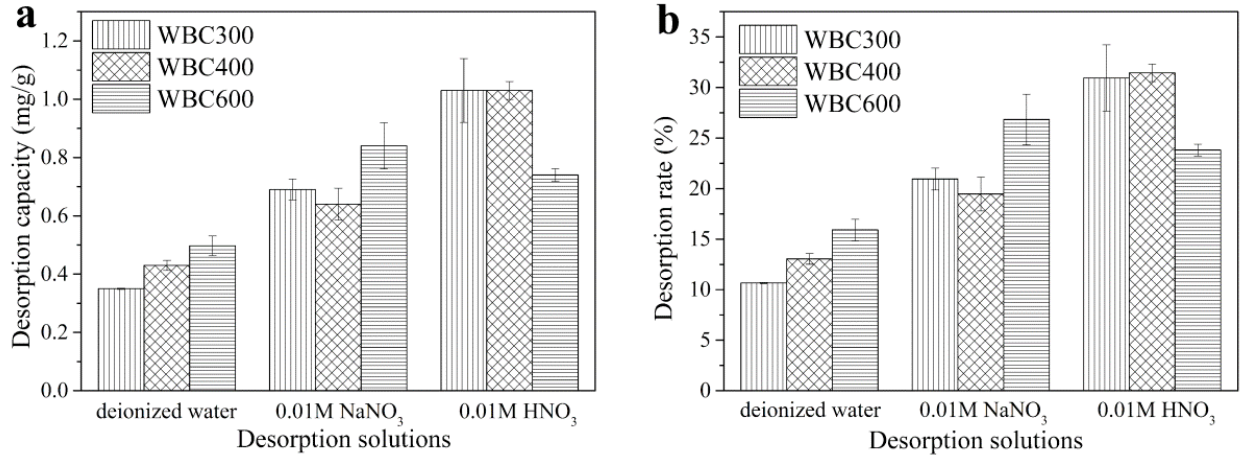

Fig. 7. (a) Desorption capacity and (b) desorption rate of different solutions for Hg(II) desorption.

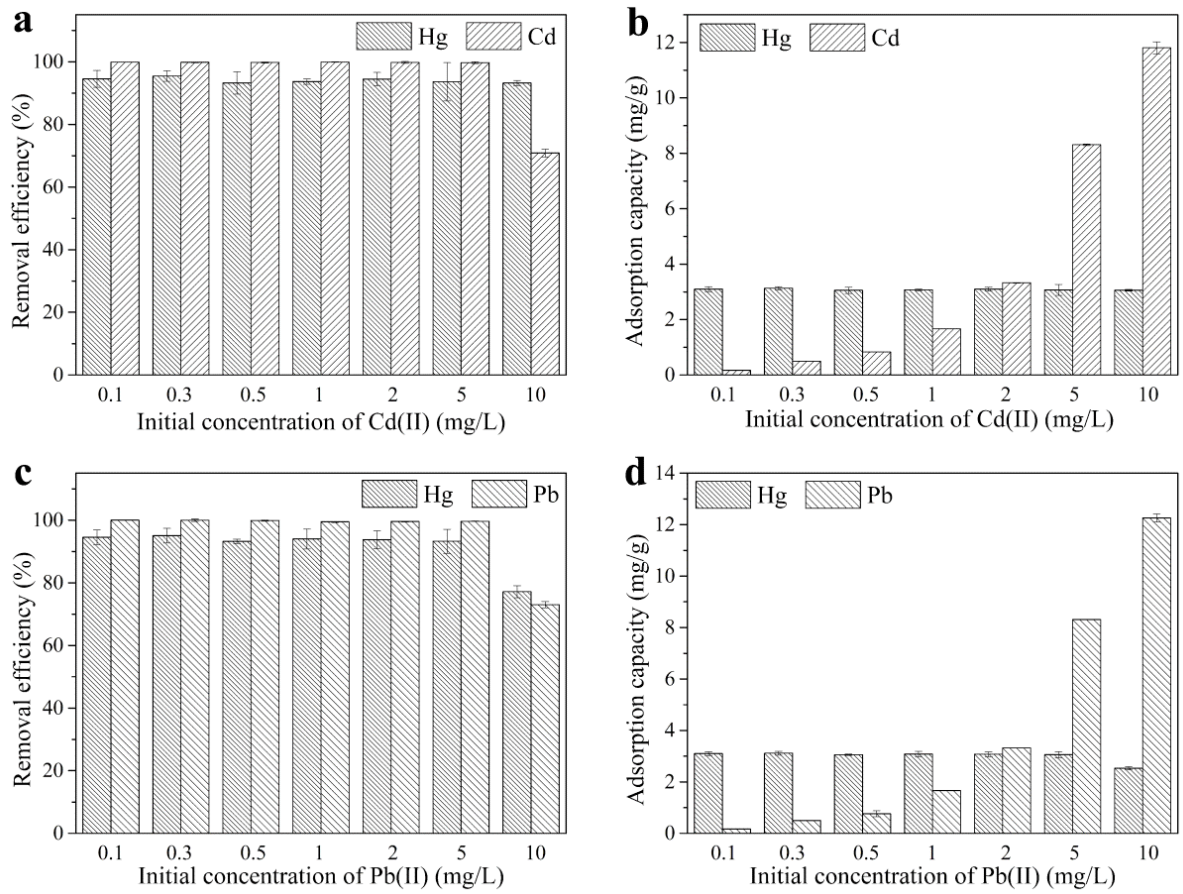

Fig. 8. (a) and (c) Removal efficiency and (b) and (d) adsorption capacity of WBC300 in binary systems.

Table 4
Equilibrium adsorption capacity in binary systems

Main adsorbates	Initial concentration of Cd(II)/Pb(II) (mg/L)						
	0.1	0.3	0.5	1	2	5	10
Hg(II)	q_e'/q_e						
Hg–Cd	0.99	1.00	0.98	0.98	0.99	0.98	0.98
Hg–Pb	0.99	1.00	0.98	0.99	0.99	0.98	0.81
Cd(II)	q_e'/q_e						
Cd–Hg	1.01	1.01	1.00	1.00	1.00	1.00	1.00
Pb(II)	q_e'/q_e						
Pb–Hg	1.00	1.00	1.03	1.00	1.00	1.00	0.97

Note: The concentration of Hg(II) in all systems was 2 mg/L.

effect influenced the adsorption reaction in binary systems. Furthermore, the effect of Pb(II) on Hg(II) was higher than that of Hg(II) on Pb(II). The reason for this phenomenon might be explained by Pb(II) and Hg(II) having partially similar adsorption sites on the biochar, and Hg(II) was uncompetitive for the active sites when the initial concentration of Pb(II) was much higher than Hg(II). Moreover, Pb(II) has two possible coordination numbers (4 and 6), as well as lager atomic number and electronegativity than Hg(II), all these factors favour the adsorption of Pb(II) by bioadsorbent [61].

3.7. Adsorption mechanism exploration

The mechanisms of metal ion adsorption are generally governed by surface chemistry and specific surface area characteristics of adsorbent [62]. Although WBC600 possessed relatively higher S_{BET}, it proved to have lower adsorption capacity than WBC300 and WBC400 which suggested that Hg(II) adsorption was not dominant determined by surface area. Previous studies manifested that coprecipitation with mineral compounds was one of the approaches for heavy metal adsorption [49], but it was excluded for WBC due to

the removal of large amount mineral compounds by water washing. Hence, for this research, functional group complexation and ion-exchange adsorption were mainly discussed for Hg(II) adsorption by these three temperature biochars. As shown in Fig. 9(a), the pH value which is required to give zero net surface charge to make adsorbent become neither positively or negatively is designated as pH_{PZC}, and all WBCs possessed high pH_{PZC}, 7.18, 7.23, and 7.58 for WBC300, WBC400, and WBC600, respectively. By observing that the equilibrium pH of both WBC300 and WBC400 was prominently lower than the initial pH in alkaline range, it can be proven that the acidic functional groups were located on the surface of biochars. It was previously mentioned that the optimum adsorption pH was 6.0 as MINTEQ model manifested that $Hg(OH)_2^{(0)}$ was the dominant species of aqueous Hg within this pH range [33], which was lower than the pH_{PZC}. Therefore, implies that the adsorption mechanism through physical forces such as electrostatic interaction was inessential because of the protonation on biochar surface at that certain pH.

Furthermore, FTIR spectra of WBCs before and after adsorption process are presented in Fig. 9(b). The three biochars all had infrared absorption peaks at 1,600 and 1,702 cm^{-1} caused by the stretching vibration bands of C=C and C=O, which could determine the presence of carboxyl combined with another stretching vibration band of O–H at 3,430 cm^{-1}. Moreover, the peak appeared at 1,091 cm^{-1} was considered to be the C–O stretching vibration, then the alcoholic hydroxyl and phenolic hydroxyl could be affirmed by associating with O–H [63]. Consequently, the carboxyl, alcoholic, and phenolic hydroxyl were obtained on the surface of WBC300 and WBC400, however, the absorption peaks weakened at 3,430, 1,702, 1,600, and 1,091 cm^{-1} after the adsorption of Hg(II) that indicated the reduction in the amount of above oxygen-containing functional groups and further demonstrating their complexations with Hg(II) to form $–COOHg^+$ and $–OHg^+$, which was evident in WBC300. The absorption peaks recorded at 2,925, 1,378, and 798 cm^{-1} were generally considered to be the stretching vibrations of hydrocarbon C–H and the scissor bending vibration of $–CH_2–$ [63]. It is further shown that with an increase in the pyrolysis temperature of biochar, comes a decrease in absorption peaks, indicating the gradual aromatization of biochars. These three weaker peaks showed no significant changes after the adsorption of Hg(II), which means they had no obvious association with the mechanism of Hg(II) removal. The functional groups in high temperature biochar WBC600 were much less than that of WBC300 and WBC400, however, only the peaks recorded at 1,600 and 1,091 cm^{-1} were weakened after Hg(II) adsorption, indicating that the complexations of Hg(II) with the oxygen-containing functional groups onto WBC600 were inconspicuous. Additionally, the results of water-soluble cation contents showed that the release of K^+ and Ca^{2+} was distinct (Table 5), and the released cation quantity of WBC600 was almost twice greater than that of WBC300 which indicated that ion-exchange was involved in Hg(II) adsorption process. On the other hand, WBC600 was more polyaromatic on the surface structure caused by higher pyrolysis temperature which was demonstrated by relative lower H/C ratios compared with WBC300 and WBC400 (Table 1). The cyclic aromatic is rich in π-donor and electron-donor which acts as a weak cation-π binder [64,65], so there was the possibility that Hg–π interaction occurred in this study, especially in WBC600. Previous research proposed that the Hg(II) adsorption followed by the redox of Hg(II) to Hg(I) by phenol, hydroquinone, and π electrons on ACs [33], but specific reduction mechanism of this biochar should be discussed in future work under advanced instruments.

4. Conclusion

In this study, biochars obtained from pyrolysis wheat straw at three different temperatures (300°C, 400°C, and 600°C) were used as adsorbent for the removal of Hg(II) in simulated wastewater. The adsorption isotherm data was well fitted to the Langmuir model ($R^2 > 0.9782$), and the adsorption kinetics data was fitted using a pseudo-second-order model ($R^2 > 0.9421$). In addition, nitric acid exhibited a relatively greater effect on Hg(II) desorption from WBC300 and WBC400 compared with WBC600, which indicated that a complexation

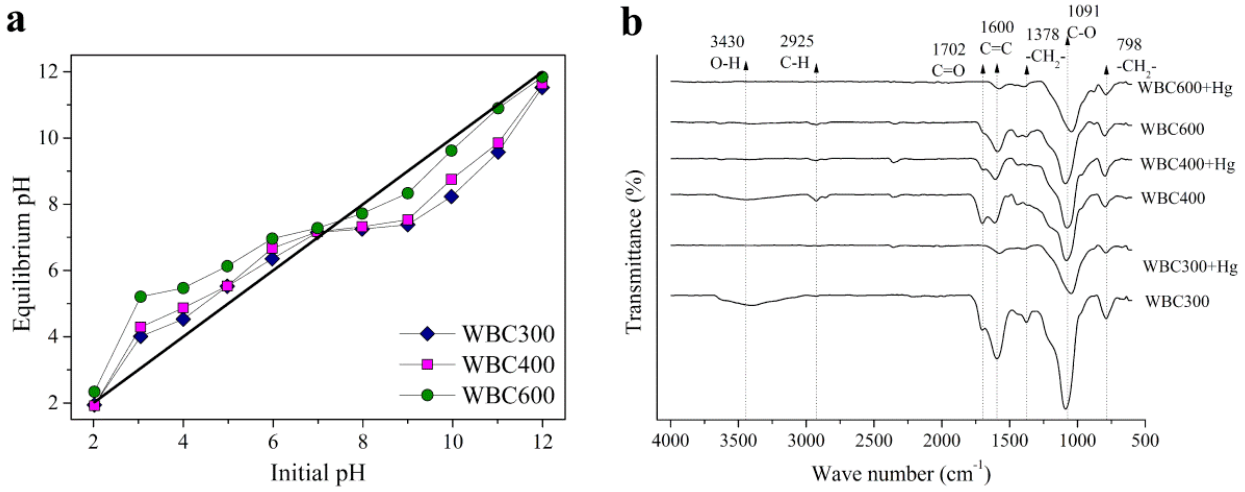

Fig. 9. (a) Point of zero charge (pH_{PZC}) curves of WBCs and (b) FTIR spectra of WBCs before and after adsorption processing.

Table 5
Content of water-soluble cations of WBCs before and after adsorption

WBCs		Concentration of cations (mg/g)			
		K^+	Na^+	Ca^{2+}	Mg^{2+}
Before adsorption	WBC300	2.70 ± 0.06	0.04 ± 0.02	0.25 ± 0.02	0.05 ± 0.01
	WBC400	2.85 ± 0.12	0.04 ± 0.02	0.24 ± 0.02	0.04 ± 0.00
	WBC600	2.52 ± 0.38	0.05 ± 0.00	0.25 ± 0.08	0.05 ± 0.01
After adsorption	WBC300	11.29 ± 0.20	0.09 ± 0.02	6.49 ± 0.38	1.45 ± 0.30
	WBC400	14.47 ± 0.25	0.09 ± 0.03	8.77 ± 0.60	2.21 ± 0.45
	WBC600	18.79 ± 0.39	0.19 ± 0.03	11.67 ± 0.82	2.37 ± 0.44
Net release quantity	WBC300	8.59 ± 0.02	0.04 ± 0.01	6.25 ± 0.46	1.41 ± 0.21
	WBC400	11.62 ± 0.06	0.04 ± 0.00	8.53 ± 0.35	2.17 ± 0.12
	WBC600	16.28 ± 0.15	0.14 ± 0.00	11.42 ± 0.07	2.31 ± 0.08

with functional groups was involved in the adsorption mechanism. Interestingly, Pb(II) competed with Hg(II) in its adsorption sites on WBC300 when presented in binary system, however, Cd(II) showed no impact on Hg(II) adsorption. It was summarized from the adsorption/desorption behaviours and characterizations that low temperature biochars (WBC300 and WBC400) adsorbed Hg(II) mainly relied on complexation reactions with carboxyl, alcoholic, and phenolic hydroxyl functional groups, while high temperature biochars (WBC600) mainly relied on ion-exchange processes, and might be accompanied by Hg–π interaction, presenting the different adsorption mechanisms from WBC300 and WBC400.

In this work, all above results demonstrated the sustainable, renewable, and inexpensive WBC as a potent adsorbent for Hg(II) removal, meanwhile it made use of an environmentally friendly adsorption mechanism without secondary pollution. The high adsorption efficiency in batch and binary systems also provided a potential method for mixed heavy metal wastewater treatment under the premise of using less amounts of adsorbent.

Acknowledgements

This research was supported by the Fuling Shale Gas Environmental Exploration Technology of National Science and Technology Special Project (Grant No.: 2016ZX05060) and the Demonstration of Integrated Management of Rocky Desertification and Enhancement of Ecological Service Function in Karst Peak-cluster Depression (Grant No.: 2016YFC0502400). All authors would like to appreciate Prof. Dr. Xujie Lu for useful suggestion and discussion.

References

[1] G. Tan, W. Sun, Y. Xu, H. Wang, N. Xu, Sorption of mercury (II) and atrazine by biochar, modified biochars and biochar based activated carbon in aqueous solution, Bioresour. Technol., 211 (2016) 727–735.
[2] M.E. Mahmoud, S.B. Ahmed, M.M. Osman, T.M. Abdel-Fattah, A novel composite of nanomagnetite-immobilized-baker's yeast on the surface of activated carbon for magnetic solid phase extraction of Hg(II), Fuel, 139 (2015) 614–621.
[3] X. Feng, P. Li, G. Qiu, S. Wang, G. Li, L. Shang, B. Meng, H. Jiang, W. Bai, Z. Li, Human exposure to methylmercury through rice intake in mercury mining areas, Guizhou Province, China, Environ. Sci. Technol., 42 (2008) 326–332.
[4] S. Mashhadi, R. Sohrabi, H. Javadian, M. Ghasemi, I. Tyagi, S. Agarwal, V.K. Gupta, Rapid removal of Hg (II) from aqueous solution by rice straw activated carbon prepared by microwave-assisted H_2SO_4 activation: kinetic, isotherm and thermodynamic studies, J. Mol. Liq., 215 (2016) 144–153.
[5] X. Dong, L.Q. Ma, Y. Zhu, Y. Li, B. Gu, Mechanistic investigation of mercury sorption by Brazilian pepper biochars of different pyrolytic temperatures based on X-ray photoelectron spectroscopy and flow calorimetry, Environ. Sci. Technol., 47 (2013) 12156–12164.
[6] L.G. Boutsika, H.K. Karapanagioti, I.D. Manariotis, Aqueous mercury sorption by biochar from malt spent rootlets, Water Air Soil Pollut., 225 (2013) 1805.
[7] Y. Lin, S. Wang, E.H. Steindal, Z. Wang, H.F. Braaten, Q. Wu, T. Larssen, A holistic perspective is needed to ensure success of minamata convention on mercury, Environ. Sci. Technol., 51 (2017) 1070–1071.
[8] D.S. Han, M. Orillano, A. Khodary, Y. Duan, B. Batchelor, A. Abdel-Wahab, Reactive iron sulfide (FeS)-supported ultrafiltration for removal of mercury (Hg(II)) from water, Water Res., 53 (2014) 310–321.
[9] J.H. Richard, C. Bischoff, C.G. Ahrens, H. Biester, Mercury (II) reduction and co-precipitation of metallic mercury on hydrous ferric oxide in contaminated groundwater, Sci. Total Environ., 539 (2016) 36–44.
[10] C.P. Nanseu-Njiki, S.R. Tchamango, P.C. Ngom, A. Darchen, E. Ngameni, Mercury(II) removal from water by electrocoagulation using aluminium and iron electrodes, J. Hazard. Mater., 168 (2009) 1430–1436.
[11] S. Vasudevan, J. Lakshmi, G. Sozhan, Optimization of electrocoagulation process for the simultaneous removal of mercury, lead, and nickel from contaminated water, Environ. Sci. Pollut. Res., 19 (2012) 2734–2744.
[12] S. Siva, S. Sudharsan, R. Sayee Kannan, Synthesis, characterization and ion-exchange properties of novel hybrid polymer nanocomposites for selective and effective mercury(II) removal, RSC Adv., 5 (2015) 79665–79678.
[13] M.A. Sinyakova, E.A. Semenova, O.A. Gamuletskaya, Ion exchange of copper(II), lanthanum(III), thallium(I), and mercury(II) on the "polysurmin" substance, Russ. J. Gen. Chem., 84 (2014) 2516–2520.
[14] L. Ernesto Amabilis-Sosa, C. Siebe, G. Moeller-Chavez, M. del Carmen Duran-Dominguez-De-Bazua, Removal of mercury by *Phragmites australis* used as biological barrier in constructed wetlans inoculated with heavy metal-tolerant strains, Rev. Int. Contam. Ambie., 32 (2016) 47–53.
[15] P. Giovanella, L. Cabral, F.M. Bento, C. Gianello, F.A. Camargo, Mercury (II) removal by resistant bacterial isolates and mercuric (II) reductase activity in a new strain of *Pseudomonas* sp. B50A, New Biotechnol., 33 (2016) 216–223.

[16] S.-J. Lee, J.H. Park, Y.-T. Ahn, J.W. Chung, Comparison of heavy metal adsorption by peat moss and peat moss-derived biochar produced under different carbonization conditions, Water Air Soil Pollut., 226 (2015) 9.
[17] T.A. Saleh, Isotherm, kinetic, and thermodynamic studies on Hg(II) adsorption from aqueous solution by silica-multiwall carbon nanotubes, Environ. Sci. Pollut. Res. Int., 22 (2015) 16721–16731.
[18] A. Gupta, S.R. Vidyarthi, N. Sankararamakrishnan, Enhanced sorption of mercury from compact fluorescent bulbs and contaminated water streams using functionalized multiwalled carbon nanotubes, J. Hazard. Mater., 274 (2014) 132–144.
[19] P. Hadi, M.H. To, C.W. Hui, C.S. Lin, G. McKay, Aqueous mercury adsorption by activated carbons, Water Res., 73 (2015) 37–55.
[20] M. Ahmad, A.U. Rajapaksha, J.E. Lim, M. Zhang, N. Bolan, D. Mohan, M. Vithanage, S.S. Lee, Y.S. Ok, Biochar as a sorbent for contaminant management in soil and water: a review, Chemosphere, 99 (2014) 19–33.
[21] M. Keiluweit, P.S. Nico, M.G. Johnson, M. Kleber, Dynamic molecular structure of plant biomass-derived black carbon (biochar), Environ. Sci. Technol., 44 (2010) 1247–1253.
[22] H. Hwang, S. Oh, T.-S. Cho, I.-G. Choi, J.W. Choi, Fast pyrolysis of potassium impregnated poplar wood and characterization of its influence on the formation as well as properties of pyrolytic products, Bioresour. Technol., 150 (2013) 359–366.
[23] K. Jindo, K. Suto, K. Matsumoto, C. García, T. Sonoki, M.A. Sanchez-Monedero, Chemical and biochemical characterisation of biochar-blended composts prepared from poultry manure, Bioresour. Technol., 110 (2012) 396–404.
[24] I.D. Manariotis, K.N. Fotopoulou, H.K. Karapanagioti, Preparation and characterization of biochar sorbents produced from malt spent rootlets, Ind. Eng. Chem. Res., 54 (2015) 9577–9584.
[25] L. Xue, B. Gao, Y. Wan, J. Fang, S. Wang, Y. Li, R. Muñoz-Carpena, L. Yang, High efficiency and selectivity of MgFe-LDH modified wheat-straw biochar in the removal of nitrate from aqueous solutions, J. Taiwan Inst. Chem. Eng., 63 (2016) 312–317.
[26] Y. Bi, Y. Wang, C. Gao, Straw resource quantity and its regional distribution in China, J. Agric. Mech. Res., 32 (2010) 1–7 (in Chinese).
[27] Z. Shen, Y. Zhang, F. Jin, O. McMillan, A. Al-Tabbaa, Qualitative and quantitative characterisation of adsorption mechanisms of lead on four biochars, Sci. Total Environ., 609 (2017) 1401–1410.
[28] Z. Shen, Y. Zhang, O. McMillan, F. Jin, A. Al-Tabbaa, Characteristics and mechanisms of nickel adsorption on biochars produced from wheat straw pellets and rice husk, Environ. Sci. Pollut. Res. Int., 24 (2017) 12809–12819.
[29] Q. Cheng, Q. Huang, S. Khan, Y. Liu, Z. Liao, G. Li, Y.S. Ok, Adsorption of Cd by peanut husks and peanut husk biochar from aqueous solutions, Ecol. Eng., 87 (2016) 240–245.
[30] J. Deng, Y. Liu, S. Liu, G. Zeng, X. Tan, B. Huang, X. Tang, S. Wang, Q. Hua, Z. Yan, Competitive adsorption of Pb(II), Cd(II) and Cu(II) onto chitosan-pyromellitic dianhydride modified biochar, J. Colloid Interface Sci., 506 (2017) 355–364.
[31] H. Jin, S. Capareda, Z. Chang, J. Gao, Y. Xu, J. Zhang, Biochar pyrolytically produced from municipal solid wastes for aqueous As(V) removal: adsorption property and its improvement with KOH activation, Bioresour. Technol., 169 (2014) 622–629.
[32] A.E. Hanandeh, R.A. Abu-Zurayk, I. Hamadneh, A.H. Al-Dujaili, Characterization of biochar prepared from slow pyrolysis of Jordanian olive oil processing solid waste and adsorption efficiency of Hg^{2+} ions in aqueous solutions, Water Sci. Technol., 74 (2016) 1899–1910.
[33] X. Xu, A. Schierz, N. Xu, X. Cao, Comparison of the characteristics and mechanisms of Hg(II) sorption by biochars and activated carbon, J. Colloid Interface Sci., 463 (2016) 55–60.
[34] H. Kong, J. He, Y. Gao, H. Wu, X. Zhu, Cosorption of phenanthrene and mercury(II) from aqueous solution by soybean stalk-based biochar, J. Agric. Food Chem., 59 (2011) 12116–12123.
[35] J. Tang, H. Lv, Y. Gong, Y. Huang, Preparation and characterization of a novel graphene/biochar composite for aqueous phenanthrene and mercury removal, Bioresour. Technol., 196 (2015) 355–363.
[36] J.S. Noh, J.A. Schwarz, Estimation of the point of zero charge of simple oxides by mass titration, J. Colloid Interface Sci., 130 (1989) 157–164.
[37] D. Prahas, Y. Kartika, N. Indraswati, S. Ismadji, Activated carbon from jackfruit peel waste by H_3PO_4 chemical activation: pore structure and surface chemistry characterization, Chem. Eng. J., 140 (2008) 32–42.
[38] J.M. Novak, I. Lima, B.S. Xing, J.W. Gaskin, C. Steiner, K.C. Das, M. Ahmedna, D. Rehrah, D.W. Watts, W.J. Busscher, Characterization of designer biochar produced at different temperatures and their effects on a loamy sand, Ann. Environ. Sci., 3 (2009) 195-206.
[39] W. Wu, J. Li, N.K. Niazi, K. Müller, Y. Chu, L. Zhang, G. Yuan, K. Lu, Z. Song, H. Wang, Influence of pyrolysis temperature on lead immobilization by chemically modified coconut fiber-derived biochars in aqueous environments, Environ. Sci. Pollut. Res., 23 (2016) 22890–22896.
[40] H. Zheng, Z. Wang, J. Zhao, S. Herbert, B. Xing, Sorption of antibiotic sulfamethoxazole varies with biochars produced at different temperatures, Environ. Pollut., 181 (2013) 60–67.
[41] D. Houben, P. Sonnet, J.-T. Cornelis, Biochar from Miscanthus: a potential silicon fertilizer, Plant Soil, 374 (2013) 871–882.
[42] J.H. Yuan, R.K. Xu, H. Zhang, The forms of alkalis in the biochar produced from crop residues at different temperatures, Bioresour. Technol., 102 (2011) 3488–3497.
[43] K.S.W. Sing, Reporting physisorption data for gas/solid systems with special reference to the determination of surface area and porosity (Recommendations 1984), Pure Appl. Chem., 57 (2009) 2201–2218.
[44] P.G. González, Y.B. Pliego-Cuervo, Adsorption of Cd(II), Hg(II) and Zn(II) from aqueous solution using mesoporous activated carbon produced from *Bambusa vulgaris* striata, Chem. Eng. Res. Des., 92 (2014) 2715–2724.
[45] P. González-García, T.A. Centeno, E. Urones-Garrote, D. Ávila-Brande, L.C. Otero-Díaz, Microstructure and surface properties of lignocellulosic-based activated carbons, Appl. Surf. Sci., 265 (2013) 731–737.
[46] P. Liu, C.J. Ptacek, D.W. Blowes, R.C. Landis, Mechanisms of mercury removal by biochars produced from different feedstocks determined using X-ray absorption spectroscopy, J. Hazard. Mater., 308 (2016) 233–242.
[47] P. Wang, L. Tang, X. Wei, G. Zeng, Y. Zhou, Y. Deng, J. Wang, Z. Xie, W. Fang, Synthesis and application of iron and zinc doped biochar for removal of p-nitrophenol in wastewater and assessment of the influence of co-existed Pb(II), Appl. Surf. Sci., 392 (2017) 391–401.
[48] Y. Han, A.A. Boateng, P.X. Qi, I.M. Lima, J. Chang, Heavy metal and phenol adsorptive properties of biochars from pyrolyzed switchgrass and woody biomass in correlation with surface properties, J. Environ. Manage., 118 (2013) 196–204.
[49] Z. Wang, G. Liu, H. Zheng, F. Li, H.H. Ngo, W. Guo, C. Liu, L. Chen, B. Xing, Investigating the mechanisms of biochar's removal of lead from solution, Bioresour. Technol., 177 (2015) 308–317.
[50] F. Yang, L. Sun, W. Xie, Q. Jiang, Y. Gao, W. Zhang, Y. Zhang, Nitrogen-functionalization biochars derived from wheat straws via molten salt synthesis: an efficient adsorbent for atrazine removal, Sci. Total Environ., 607–608 (2017) 1391–1399.
[51] W. Yang, Y. Liu, Q. Wang, J. Pan, Removal of elemental mercury from flue gas using wheat straw chars modified by Mn-Ce mixed oxides with ultrasonic-assisted impregnation, Chem. Eng. J., 326 (2017) 169–181.
[52] A. Trubetskaya, P.A. Jensen, A.D. Jensen, M. Steibel, H. Spliethoff, P. Glarborg, F.H. Larsen, Comparison of high temperature chars of wheat straw and rice husk with respect to chemistry, morphology and reactivity, Biomass Bioenergy, 86 (2016) 76–87.
[53] S. Schaefer, G. Muñiz, M.T. Izquierdo, S. Mathieu, M.L. Ballinas-Casarrubias, G. González-Sánchez, A. Celzard, V. Fierro, Rice straw-based activated carbons doped with SiC for enhanced hydrogen adsorption, Int. J. Hydrogen Energy, 42 (2017) 11534–11540.

[54] L. Cui, Y. Wang, L. Gao, L. Hu, Q. Wei, B. Du, Removal of Hg(II) from aqueous solution by resin loaded magnetic beta-cyclodextrin bead and graphene oxide sheet: synthesis, adsorption mechanism and separation properties, J. Colloid Interface Sci., 456 (2015) 42–49.
[55] K.V. Kumar, V. Ramamurthi, S. Sivanesan, Modeling the mechanism involved during the sorption of methylene blue onto fly ash, J. Colloid Interface Sci., 284 (2005) 14–21.
[56] K.C. Bedin, A.C. Martins, A.L. Cazetta, O. Pezoti, V.C. Almeida, KOH-activated carbon prepared from sucrose spherical carbon: adsorption equilibrium, kinetic and thermodynamic studies for Methylene Blue removal, Chem. Eng. J., 286 (2016) 476–484.
[57] L. Deng, Z. Shi, L. Wang, S. Zhou, Fabrication of a novel $NiFe_2O_4$/Zn-Al layered double hydroxide intercalated with EDTA composite and its adsorption behavior for Cr(VI) from aqueous solution, J. Phys. Chem. Solids, 104 (2017) 79–90.
[58] H. Raghubanshi, S.M. Ngobeni, A.O. Osikoya, N.D. Shooto, C.W. Dikio, E.B. Naidoo, E.D. Dikio, R.K. Pandey, R. Prakash, Synthesis of graphene oxide and its application for the adsorption of Pb^{+2} from aqueous solution, J. Ind. Eng. Chem., 47 (2017) 169–178.
[59] D. Kołodyńska, J. Krukowska, P. Thomas, Comparison of sorption and desorption studies of heavy metal ions from biochar and commercial active carbon, Chem. Eng. J., 307 (2017) 353–363.
[60] T. Wang, H. Sun, Biosorption of heavy metals from aqueous solution by UV-mutant *Bacillus subtilis*, Environ. Sci. Pollut. Res. Int., 20 (2013) 7450–7463.
[61] A.B. Perez-Marin, A. Ballester, F. Gonzalez, M.L. Blazquez, J.A. Munoz, J. Saez, V.M. Zapata, Study of cadmium, zinc and lead biosorption by orange wastes using the subsequent addition method, Bioresour. Technol., 99 (2008) 8101–8106.
[62] J.-H. Zhou, Z.-J. Sui, J. Zhu, P. Li, D. Chen, Y.-C. Dai, W.-K. Yuan, Characterization of surface oxygen complexes on carbon nanofibers by TPD, XPS and FT-IR, Carbon, 45 (2007) 785–796.
[63] P. Srinivasan, A.K. Sarmah, R. Smernik, O. Das, M. Farid, W. Gao, A feasibility study of agricultural and sewage biomass as biochar, bioenergy and biocomposite feedstock: production, characterization and potential applications, Sci. Total Environ., 512–513 (2015) 495–505.
[64] M. Keiluweit, M. Kleber, Molecular-level interactions in soils and sediments: the role of aromatic π-systems, Environ. Sci. Technol., 43 (2009) 3421–3429.
[65] D. Da, The cation-π interaction, Acc. Chem. Res., 46 (2013) 885–893.